The peak associated with the highest eKE in the spectrum is found beyond the energetic limit for fragmentation into OH + HF ground state products. These events must result from direct photodetachment into the exit channel FH–OH vdW complex of the F + H_2O reaction. A higher-lying HF–HO vdW complex in the exit channel may be responsible for the lower-energy peak at 1.0 eV (*19*). Another feature is observed at 0.45 eV, roughly one vibrational quantum in HF (~0.6 eV) above the FH–OH vdW complex. Corresponding features observed in the dissociative PPC spectrum in Fig. 2 suggest that this signal arises from a temporarily trapped vdW complex, FH(v′ = 1)–OH, a long-lived Feshbach resonance.

To understand the nature of the stable spectrum, the energy spectrum of the remaining wave packet after 2.5-ps propagation was computed. The calculated spectrum is compared in Fig. 3 with the experiment. The features centered around 0.55 and 0.15 eV are attributed to long-lived Feshbach resonances trapped in the FH(v′ = 1,2)–OH vdW wells, with representative wave functions illustrated in Fig. 1. Given that the experimental spectrum represents states with far longer lifetimes (5 μs) than is tractable to theoretically compute, the agreement is quite reasonable. An intriguing finding is the peak at 0.05 eV in the calculated stable spectrum. A closer inspection of the coincidence plot in Fig. 2A reveals a corresponding horizontal feature at the same eKE, corresponding to events distributed between KER = 0 to 0.4 eV. The appearance of this feature in conjunction with the peak observed in the stable spectrum can be interpreted in terms of a metastable state that is formed in the DPD process [e.g., an FH(v′ = 2)–OH Feshbach resonance] and therefore has a fixed electron spectrum. However, as this state decays on its way to the detector, the delayed fragmentation process over a nanosecond-microsecond time scale leads to an underestimation of the KER of the fragments, resulting in a horizontal band structure.

The wide range of observables simultaneously captured in the PPC experiment reported here provides a critical test for the accurate description of both the PESs and reaction dynamics over a wide range of translational and internal energies. Both lowest-lying electronic states play an active role in the dissociation process and must be taken into account to understand the nature of the FH_2O dissociation. Long-lived Feshbach resonances have been found in this four-atom system, experimentally and theoretically. Although very good overall agreement has been achieved between experiment and theory, challenges remain. The discrepancies found in the contribution of the A state, as well as the energetic positions and nature of the Feshbach resonance states, demand further studies of this new benchmark reaction.

References and Notes

1. W. Dong *et al*., *Science* **327**, 1501–1502 (2010).
2. M. Qiu *et al*., *Science* **311**, 1440–1443 (2006).
3. C. Xiao *et al*., *Science* **333**, 440–442 (2011).
4. R. Brownsword, M. Hillenkamp, P. Schmiechen, H. Volpp, J. Wolfrum, *Chem. Phys. Lett.* **275**, 325–331 (1997).
5. S. Liu, X. Xu, D. H. Zhang, *J. Chem. Phys.* **136**, 144302 (2012).
6. M. Alagia *et al*., *Chem. Phys.* **207**, 389–409 (1996).
7. D. Clary, *J. Chem. Phys.* **96**, 3656–3665 (1992).
8. S. Yan, Y. T. Wu, B. Zhang, X. F. Yue, K. Liu, *Science* **316**, 1723–1726 (2007).
9. S. A. Harich *et al*., *Nature* **419**, 281–284 (2002).
10. X. Wang *et al*., *Science* **322**, 573–576 (2008).
11. L. Che *et al*., *Science* **317**, 1061–1064 (2007).
12. D. M. Neumark, *J. Chem. Phys.* **125**, 132303 (2006).
13. E. Garand, J. Zhou, D. E. Manolopoulos, M. H. Alexander, D. M. Neumark, *Science* **319**, 72–75 (2008).
14. D. E. Manolopoulos *et al*., *Science* **262**, 1852–1855 (1993).
15. P. Ricaud, F. Lefèvre, *Adv. Fluorine Sci.* **1**, 1–32 (2006).
16. D. A. Neufeld, J. Zmuidzinas, P. Schilke, T. G. Phillips, *Astrophys. J. Lett.* **488**, L141–L144 (1997).
17. M. P. Deskevich, D. J. Nesbitt, H.-J. Werner, *J. Chem. Phys.* **120**, 7281–7289 (2004).
18. J. Li, R. Dawes, H. Guo, *J. Chem. Phys.* **137**, 094304 (2012).
19. J. Li, B. Jiang, H. Guo, *J. Chem. Phys.* **138**, 074309 (2013).
20. J. Li, B. Jiang, H. Guo, *Chem. Sci.* **4**, 629–632 (2013).
21. P. S. Stevens, W. H. Brune, J. G. Anderson, *J. Phys. Chem.* **93**, 4068–4079 (1989).
22. X. Yang, X.-B. Wang, L.-S. Wang, *J. Chem. Phys.* **115**, 2889–2892 (2001).
23. Y. Ishikawa, T. Nakajima, T. Yanai, K. Hirao, *Chem. Phys. Lett.* **363**, 458–464 (2002).
24. M. Ziemkiewicz, M. Wojcik, D. J. Nesbitt, *J. Chem. Phys.* **123**, 224307 (2005).
25. M. Ziemkiewicz, D. J. Nesbitt, *J. Chem. Phys.* **131**, 054309 (2009).
26. A. M. Zolot, D. J. Nesbitt, *J. Chem. Phys.* **129**, 184305 (2008).
27. C. J. Johnson, B. B. Shen, B. L. J. Poad, R. E. Continetti, *Rev. Sci. Instrum.* **82**, 105105–105105 (2011).
28. R. E. Continetti, *Annu. Rev. Phys. Chem.* **52**, 165–192 (2001).
29. The energetics are estimated from the dissociation energy (1.136 eV) of $F^-(H_2O)$ (*30*) to form F^- + H_2O, the experimental ionization energy of F^- (3.401 eV) (*31*) to reach the F + H_2O product asymptote, and the reaction enthalpy (17.6 kcal/mol) (*26*) for the F + H_2O reaction.
30. P. Weis, P. R. Kemper, M. T. Bowers, S. S. Xantheas, *J. Am. Chem. Soc.* **121**, 3531–3532 (1999).
31. C. Blondel, P. Cacciani, C. Delsart, R. Trainham, *Phys. Rev. A* **40**, 3698–3701 (1989).

Acknowledgments: This work was supported by the U.S. Department of Energy (DE-FG03-98ER14879 to R.E.C. and DE-FG02-05ER15694 to H.G.). R.O. thanks the German Academic Exchange Service (DAAD) for a postdoctoral research fellowship. J.M. thanks the National Natural Science Foundation of China (21303110) for partial support.

Supplementary Materials

www.sciencemag.org/content/343/6169/396/suppl/DC1
Materials and Methods
Figs. S1 to S5
Tables S1 to S4
References (*32*–*47*)

21 October 2013; accepted 13 December 2013
Published online 9 January 2014;
10.1126/science.1247424

Strong Ground Motion Prediction Using Virtual Earthquakes

M. A. Denolle,[1,2] E. M. Dunham,[1,3] G. A. Prieto,[4] G. C. Beroza[1]

Sedimentary basins increase the damaging effects of earthquakes by trapping and amplifying seismic waves. Simulations of seismic wave propagation in sedimentary basins capture this effect; however, there exists no method to validate these results for earthquakes that have not yet occurred. We present a new approach for ground motion prediction that uses the ambient seismic field. We apply our method to a suite of magnitude 7 scenario earthquakes on the southern San Andreas fault and compare our ground motion predictions with simulations. Both methods find strong amplification and coupling of source and structure effects, but they predict substantially different shaking patterns across the Los Angeles Basin. The virtual earthquake approach provides a new approach for predicting long-period strong ground motion.

Sedimentary basins amplify and extend the duration of strong shaking from earthquakes (*1*). State-of-the-art simulations of wave propagation for scenario earthquakes through crustal structures that include sedimentary basins explore these effects (*2*–*7*). Evidence that strong basin amplification in Los Angeles for earthquakes that would occur on the southern San Andreas fault emerged from such ground motion simulations (*3*, *7*), but because of the absence of recent earthquakes large enough to excite long-period seismic waves, they have not been validated with observations. Our study was motivated by the need to validate these simulations, which, if correct, would greatly increase seismic hazard.

To validate ground motion simulations without recordings of large earthquakes, we developed

[1]Department of Geophysics, Stanford University, 397 Panama Mall, Stanford, CA 94305, USA. [2]Scripps Institution of Oceanography, University of California, San Diego, La Jolla, CA 92093, USA. [3]Institute for Computational and Mathematical Engineering, Stanford University, Stanford, CA 94305, USA. [4]Department of Earth, Atmospheric and Planetary Science, Massachusetts Institute of Technology, 77 Massachusetts Avenue, Cambridge, MA 02139, USA.
*Corresponding author. E-mail: mdenolle@stanford.edu.

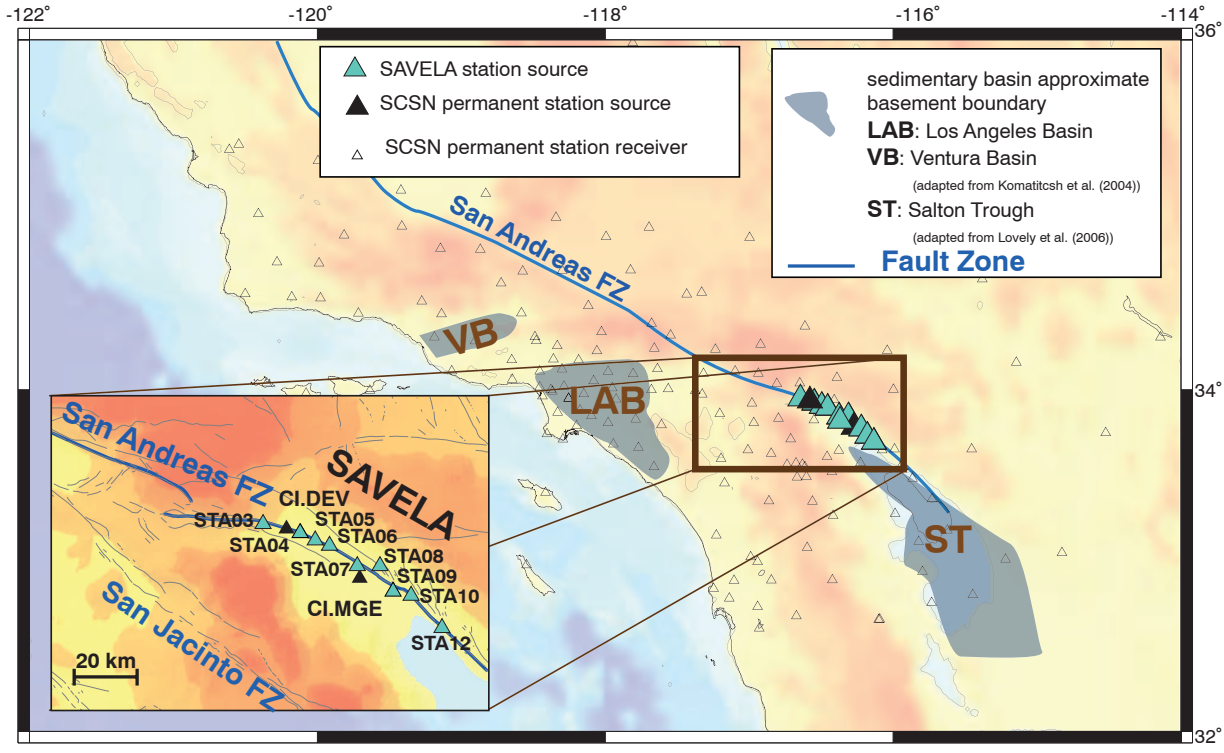

Fig. 1. Temporary SAVELA and permanent Southern California Seismic Network (SCSN) stations. Shaded area shows the approximate shape of major sedimentary basins. Open triangles are SCSN seismic stations that we treat as receivers. Filled triangles are seismic stations with temporary deployments (blue) and permanent SCSN (black) stations near the San Andreas fault that we treat as virtual sources. San Andreas fault zone (solid blue lines) and quaternary faults location from http://earthquakes.usgs.gov/hazards/qfaults. SAVELA stations are located within 3 km of the fault trace (bottom left inset).

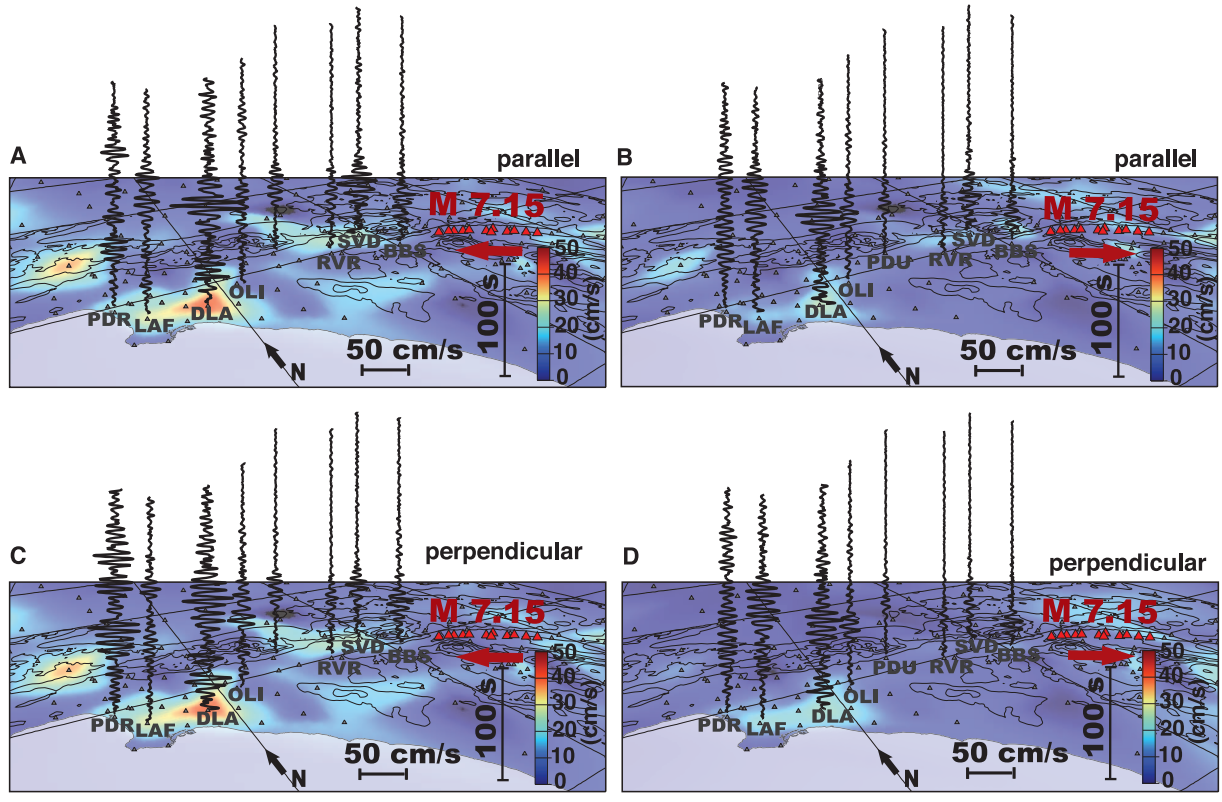

Fig. 2. Seismic amplification in sedimentary basin and waveguide effect. Velocity seismograms (black waveforms) and PGV (color scale) for two M 7.15 scenario earthquake ruptures determined using the VEA. Simulations are divided into northwestward-propagating ruptures (**A** and **C**) and southeastward-propagating ruptures (**B** and **D**) for the horizontal fault-parallel (A and B) and fault-perpendicular (C and D) components of motion. Seismic amplification appears at all cases but is stronger for northwestward rupture that produces up to two times more shaking than the southeastward rupture.

a Virtual Earthquake Approach (VEA) that models long-period strong ground motion using Green's functions derived from the ambient seismic field (fig. S1). The ambient seismic field is excited by the coupling of the oceans and atmosphere with the solid Earth and carries the signature of the structure between two seismic stations. It is possible to extract the Earth's response to an impulsive force (i.e., the Green's function) through correlation of the ambient seismic field (*8*–*15*). This capability has enabled the imaging of the Earth's wave speed structure through travel-time measurements (*16*, *17*). The ambient seismic field also contains amplitude information, which has been used to measure anelastic effects (*18*, *19*) and which we exploit to predict earthquake ground motion intensity.

Ambient seismic field Green's functions reproduce waveform shapes and relative amplitudes of earthquakes for nearby stations (*20*). Once the Green's functions are corrected from a surface point-force source to a double-couple source at depth, the agreement between real-earthquake and virtual-earthquake waveforms systematically improves (*21*). Here, we extended this method from point sources, appropriate for moderate magnitude (M ~5) earthquakes, to finite ruptures of larger magnitude using the representation theorem (*22*).

We applied this technique to predict ground motion in greater Los Angeles for scenario earthquakes on the San Andreas fault. To support this effort, we deployed a temporary array of broadband seismometers along the fault to determine the Green's functions for virtual sources along that segment (Fig. 1). We refer to our experiment as SAVELA (San Andreas Virtual Earthquake—Los Angeles). We corrected the ambient-field Green's functions for source location, depth, and mechanism using our understanding of the surface-wave excitation local to the virtual source (*23*–*25*). We then calculated seismograms using the VEA for a suite of M ~7 scenario earthquakes along the fault and compared the results with simulations of wave propagation through three-dimensional models of the Earth's crust (*6*). We explain the details of the method in the supplementary materials.

The source of the ambient seismic field is not uniformly distributed with azimuth (*26*), and different components of motion (S_H and P-S_v) are not equally excited. Both of these factors affect the recovered amplitude. We corrected our Green's functions to compensate for a first-order azimuthal pattern as follows. For each source component (vertical, radial, and transverse), we find sinusoidal functions that best match the observed variation with azimuth of the Green's function amplitudes (fig. S2). For each component, we estimated the calibration factor required for the ambient-field data to predict observed amplitudes for two local moderate events—the 2008 M 5.4 Chino Hills and 2008 M 5.1 Hector Road earthquakes.

We considered an ensemble of 96 magnitude 7.15 simulated ruptures developed for this segment of the fault. This represents a small subset of pseudodynamic (*27*) models developed for the CyberShake project (*6*). The kinematic source model describes fault rupture as a collection of

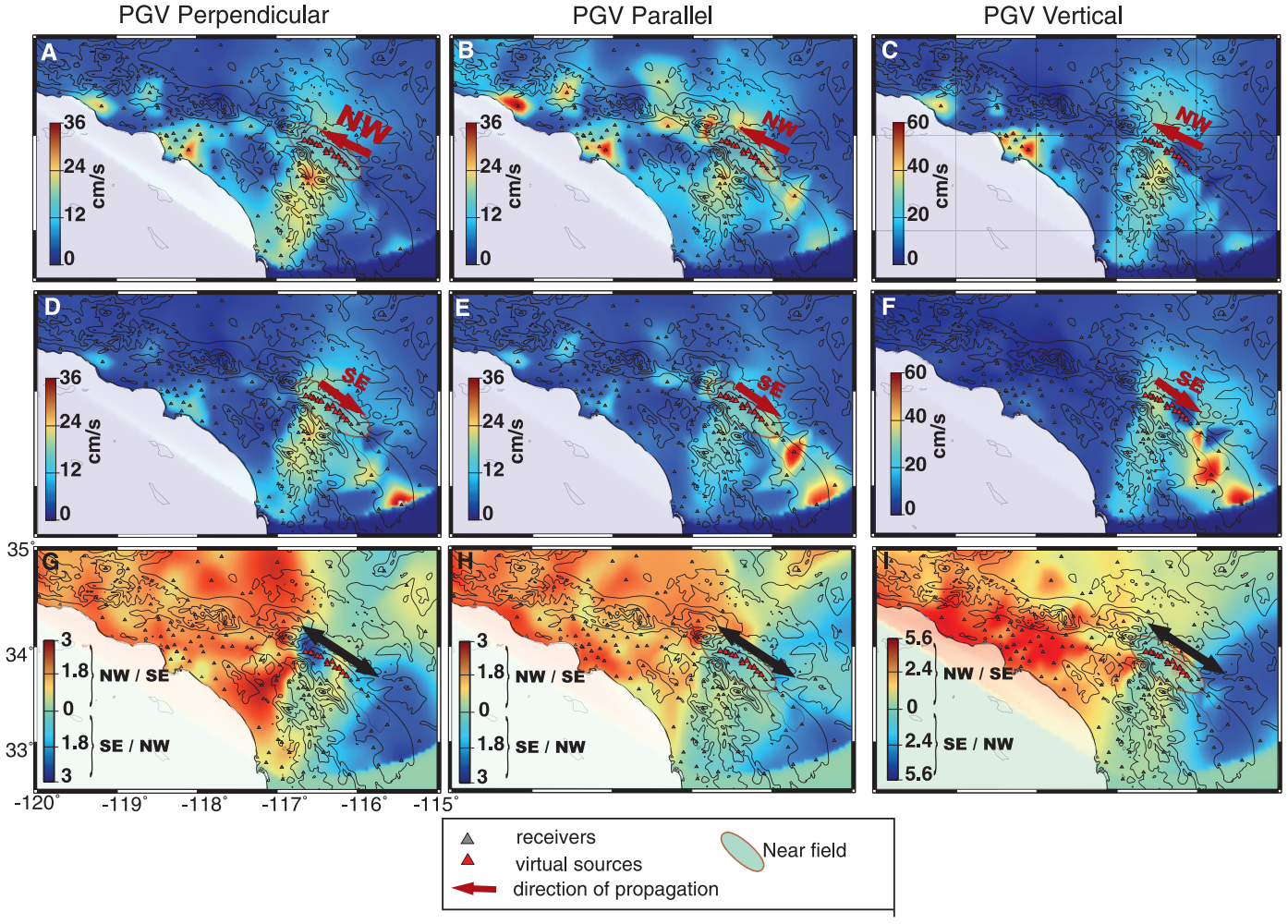

Fig. 3. Coupling of source-directivity and basin structure. PGV averaged over all northwestward-NW (**A** to **C**) and southeastward-NE (**D** to **F**) propagating ruptures for perpendicular-to-strike (A and D), parallel-to-strike (B and E), and vertical (C and F) components of motion. Los Angeles sedimentary basin experiences seismic amplification in all cases, and the effect is stronger for the parallel components. (**G** to **I**) Ratio of averaged peak amplitudes of NW-over-SE propagating ruptures. (G to I) Warm colors show how many times the NW ruptures enhance the shaking as compared to the SE ruptures.

point sources that represents square fault patches of 1-km^2 area. We use the VEA correction to account for depth, mechanism, and timing of each. We convolve the waveform with the source time function of individual sources and sum the contributions from all point sources to form the entire source. We compare long-period ground motion predictions that result from our VEA with the CyberShake simulations.

Our ground motion predictions show strong seismic amplification in the Los Angeles sedimentary basin compared to surrounding areas (Fig. 2). We compare the effect of unilateral rupture for a given slip distribution, by assuming hypocenters located at the southern and northern ends of the segment. In both cases, we find seismic amplification in downtown Los Angeles with peak amplitudes up to three times larger than in surrounding areas. The pattern of peak ground motion and the persistence of the amplification in both predictions reflect the presence of a waveguide that funnels seismic waves from west of San Gorgonio Pass to downtown Los Angeles. The amplification is more pronounced for the rupture propagating toward the basin, and in this example, the ratio of predicted peak velocities is approximately three. This contrast is less than predicted by the TeraShake simulations (*3*) and may result from the fact that the *M* 7.7 TeraShake source model ruptured a much greater fault length.

Ensembles of slip distributions that have hypocenters located at either end of the fault segment show a similar source-directivity effect on ground motion (Fig. 3). Amplification in sedimentary basins appears clearly in all cases. Our results again show peak amplitudes in Los Angeles that are, on average, three times those of the surroundings (Fig. 3). The long-period peak ground velocity (PGV) averaged over all scenarios, experienced in downtown Los Angeles, is as high as 50 cm/s for the vertical and 36 cm/s for the horizontal components. This differs substantially from the strong ground motion amplitudes at higher frequencies and closer distances where horizontal amplitudes are typically larger than vertical amplitudes (*28*).

We construct Green's functions for a laterally homogeneous medium (*25*) and find a systematic variation of the amplitudes that approximates a dipole (supplementary text and fig. S3). We contrast this with the behavior for virtual-earthquake seismograms, from which we see strong variations of amplitude ratios for all three components of motion (Fig. 3). The strength of the directivity-structure coupling is not only larger than for the laterally homogeneous case but is more extensive and spatially variable. The coupling between source directivity and basin structure (*6*) appears in the enhanced amplification in both the Ventura and Los Angeles basins. Northern Los Angeles and the San Gabriel foothills experience strong coupling on the strike-perpendicular component, whereas the coupling of the parallel component is stronger in South Los Angeles, Palos Verdes, and Chino Hills. Coupling of the vertical component

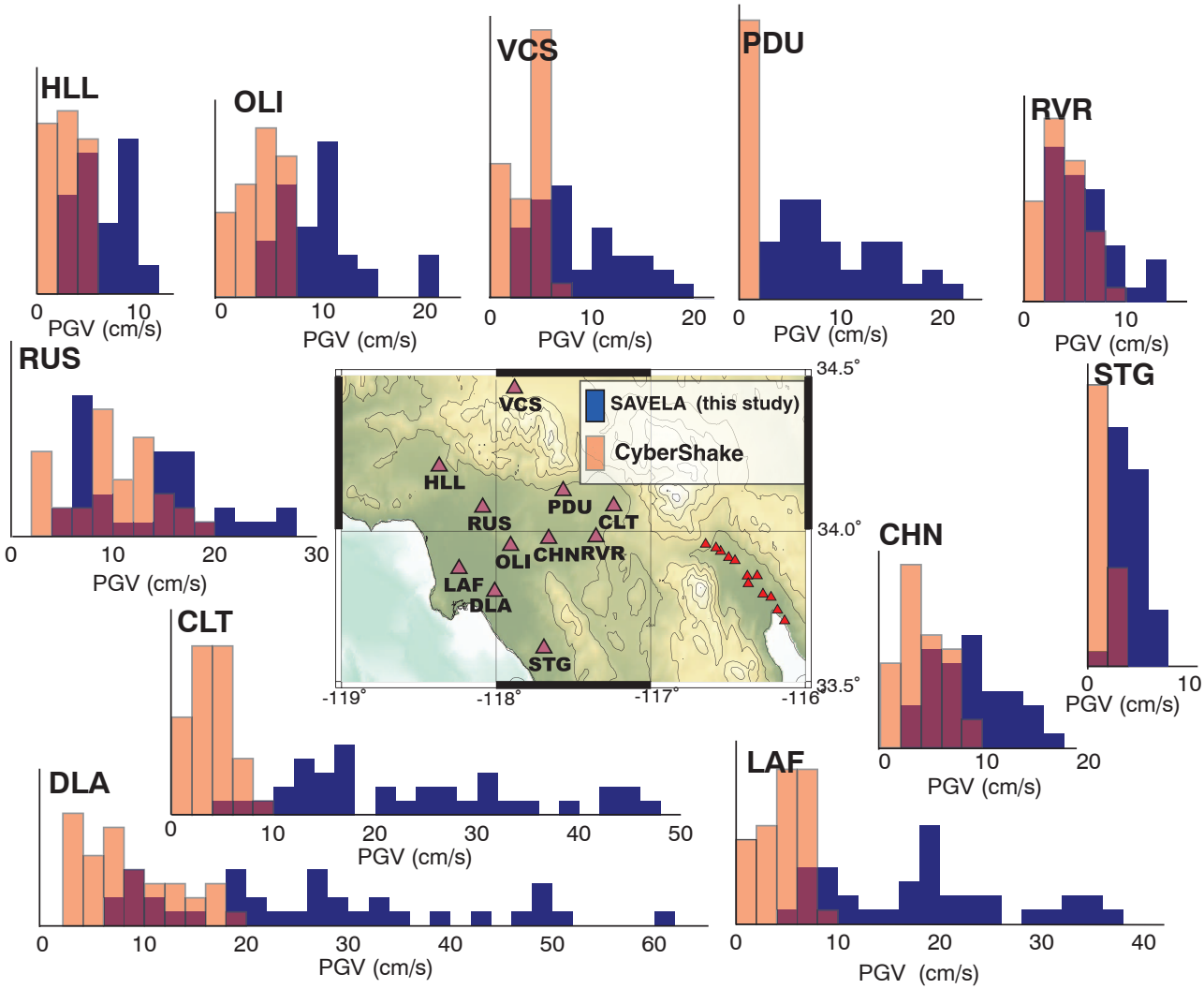

Fig. 4. Cross-validation of simulations (CyberShake) and the VEA (SAVELA). Histograms of PGV (*y* axis, number of scenario earthquakes) for all 36 tested scenarios for CyberShake (orange) and SAVELA (blue) for particular sites in Los Angeles Basin. SAVELA predicts equal shaking for RUS, RVR, and HLL and predicts larger shaking in particular for sites in the basin (LAF, DLA, CHN, CLT, and STG). The variability of the ground motion increases with intensity of shaking.

correlates with the deepest part of the sedimentary basin.

The predicted ground motion is qualitatively similar for the VEA and CyberShake simulations (figs. S4 and S5); however, there are substantial quantitative differences in the level and distribution of the shaking (Fig. 4). SAVELA results show stronger shaking than CyberShake at most sites. This is especially true for receivers in the basin. We note that both methods are subject to substantial uncertainties. The accuracy of the CyberShake simulations depends strongly on the accuracy of the assumed crustal velocity model and its derived Green's functions. The accuracy of the virtual earthquake results depends strongly both on the accuracy of the ambient-field Green's functions and on the accuracy of the amplitude calibration. The Green's functions we used for this study (fig. S1) would be more accurate if we had data from a longer deployment. To estimate the variability in PGV due to the amplitude calibration described above, we measure the maximum difference in predicted PGV when using the calibration from either the Hector Road or Chino Hills earthquake to the mean of the calibration used in this study. The variability that results is bounded at 10 cm/s for our simulations. For both the virtual earthquake and CyberShake simulations, the variation of the PGV is narrow for stations with low PGV values (bedrock sites) and wide for stations with high PGV values (basin sites). The coefficient of variation is approximately constant for SAVELA (fig. S7), which indicates that variability increases proportionally with ground motion amplitude.

Nonlinear effects in shallow materials are important in strong ground motion. Ground motion simulations that have incorporated nonlinear soil effects (*29*) have found a large decrease in the predicted strong ground motion. This could be an important effect for the scenarios we consider because unconsolidated sediments are likely to be found in sedimentary basins and would be expected to behave nonlinearly during strong shaking. We calibrated the amplitudes of the Green's functions, such that the peak amplitudes predicted by our approach matched those of moderate-sized earthquakes. Our approach, as well as the CyberShake simulations, is based on an assumption of linearity. To the extent that nonlinear effects are important, our predicted ground motion amplitudes are likely to overestimate true amplitudes in future large earthquakes.

We confirm the presence and the influence of a waveguide to the west of San Gorgonio Pass that funnels seismic waves from San Andreas fault events into the Los Angeles Basin. This amplification is present for all tested scenarios. We also confirm that directivity couples with shallow crustal structure to increase basin amplification (*6*). We find a constant coefficient of variation, which means that shaking variability is proportional to shaking intensity. We also find a wider range of predicted peak amplitudes than is found in simulations, which would increase uncertainty in ground motion predictions and thereby impact seismic hazard assessments. We note, however, that there are substantial uncertainties in our estimated Green's functions and their amplitude calibration. Moreover, station coverage in the basin is sparse, and we have only sampled a small portion of the variability expected for a complex wavefield in the basin. Our results support more ambitious, targeted experiments to improve the accuracy of long-period strong ground motion prediction for future earthquakes in regions subject to high seismic risk.

References and Notes

1. P.-Y. Bard, M. Campillo, F. J. Chávez-Garcia, F. J. Sánchez-Sesma, *Earthq. Spectra* **4**, 609–633 (1988).
2. K. B. Olsen, R. J. Archuleta, J. R. Matarese, *Science* **270**, 1628–1632 (1995).
3. K. Olsen *et al.*, *Geophys. Res. Lett.* **33**, L07305 (2006).
4. K. B. Olsen *et al.*, *Geophys. Res. Lett.* **36**, L04303 (2009).
5. K. B. Olsen, *Bull. Seismol. Soc. Am.* **90** (6B), S77–S94 (2000).
6. R. Graves *et al.*, *Pure Appl. Geophys.* **168**, 367–381 (2011).
7. S. M. Day, D. Roten, K. B. Olsen, *Geophys. J. Int.* **189**, 1103–1124 (2012).
8. K. Aki, *Bull. Earthq. Res. I. Tokyo* **35**, 415 (1957).
9. J. Claerbout, *Geophysics* **33**, 264–269 (1968).
10. O. I. Lobkis, R. L. Weaver, *J. Acoust. Soc. Am.* **110**, 3011 (2001).
11. R. L. Weaver, O. I. Lobkis, *Geophysics* **71**, S15 (2006).
12. F. J. Sánchez-Sesma, M. Campillo, *Bull. Seismol. Soc. Am.* **96**, 1182–1191 (2006).
13. M. Campillo, A. Paul, *Science* **299**, 547–549 (2003).
14. N. M. Shapiro, M. Campillo, *Geophys. Res. Lett.* **31**, L07614 (2004).
15. K. G. Sabra, P. Gerstoft, P. Roux, W. A. Kuperman, M. C. Fehler, *Geophys. Res. Lett.* **32**, L03310 (2005).
16. N. M. Shapiro, M. Campillo, L. Stehly, M. H. Ritzwoller, *Science* **307**, 1615–1618 (2005).
17. K. Nishida, H. Kawakatsu, K. Obara, *J. Geophys. Res.* **113** (B10), B10302 (2008).
18. G. A. Prieto, J. F. Lawrence, G. C. Beroza, *J. Geophys. Res.* **114** (B7), B07303 (2009).
19. G. A. Prieto, M. Denolle, J. F. Lawrence, G. C. Beroza, *C. R. Geosci.* **343**, 600–614 (2011).
20. G. A. Prieto, G. C. Beroza, *Geophys. Res. Lett.* **35**, L14304 (2008).
21. M. A. Denolle, E. M. Dunham, G. A. Prieto, G. C. Beroza, *J. Geophys. Res.* **118**, 2102 (2013).
22. R. Burridge, L. Knopoff, *Bull. Seismol. Soc. Am.* **54**, 1875–1888 (1964).
23. H. Magistrale, S. Day, R. W. Clayton, R. Graves, *Bull. Seismol. Soc. Am.* **90** (6B), S65–S76 (2000).
24. M. D. Kohler, H. Magistrale, R. W. Clayton, *Bull. Seismol. Soc. Am.* **93**, 757–774 (2003).
25. M. A. Denolle, E. M. Dunham, G. C. Beroza, *Bull. Seismol. Soc. Am.* **102**, 1214–1223 (2012).
26. L. Stehly, M. Campillo, N. Shapiro, *J. Geophys. Res.* **111** (B10), B10306 (2006).
27. M. Guatteri, P. M. Mai, G. C. Beroza, *Bull. Seismol. Soc. Am.* **94**, 2051–2063 (2004).
28. K. W. Campbell, Y. Bozorgnia, *Bull. Seismol. Soc. Am.* **93**, 314–331 (2003).
29. D. Roten, K. B. Olsen, J. C. Pechmann, *Bull. Seismol. Soc. Am.* **102**, 2008–2030 (2012).

Acknowledgments: We thank K. Olsen and anonymous reviewers for their comments and contributions to improve the manuscript. This work was supported by NSF grant EAR-0943885 and by the Southern California Earthquake Center (SCEC). SCEC is funded by NSF cooperative agreement EAR-0529922 and U.S. Geological Survey cooperative agreement 07HQAG0008. The SCEC contribution number for this paper is 1812. Data are available in the supplementary materials.

Supplementary Materials

www.sciencemag.org/content/343/6169/399/suppl/DC1
Materials and Methods
Figs. S1 to S7
References (*30*–*33*)

9 September 2013; accepted 19 December 2013
10.1126/science.1245678

Increased Dust Deposition in the Pacific Southern Ocean During Glacial Periods

F. Lamy,[1,2]* R. Gersonde,[1,2] G. Winckler,[3,4] O. Esper,[1] A. Jaeschke,[1,2] G. Kuhn,[1] J. Ullermann,[1] A. Martinez-Garcia,[5] F. Lambert,[6] R. Kilian[7]

Dust deposition in the Southern Ocean constitutes a critical modulator of past global climate variability, but how it has varied temporally and geographically is underdetermined. Here, we present data sets of glacial-interglacial dust-supply cycles from the largest Southern Ocean sector, the polar South Pacific, indicating three times higher dust deposition during glacial periods than during interglacials for the past million years. Although the most likely dust source for the South Pacific is Australia and New Zealand, the glacial-interglacial pattern and timing of lithogenic sediment deposition is similar to dust records from Antarctica and the South Atlantic dominated by Patagonian sources. These similarities imply large-scale common climate forcings, such as latitudinal shifts of the southern westerlies and regionally enhanced glaciogenic dust mobilization in New Zealand and Patagonia.

Mineral aerosols (dust) play a crucial role in determining the pattern and magnitude of climate variability. Dust impurities trapped in Antarctic ice point to ~25 times higher glacial dust fluxes compared with interglacials (*1*). It has been suggested that an increase

Strong Ground Motion Prediction Using Virtual Earthquakes

M. A. Denolle *et al.*

Science **343**, 399 (2014);
DOI: 10.1126/science.1245678

Science (print ISSN 0036-8075; online ISSN 1095-9203) is published weekly, except the last week in December, by the American Association for the Advancement of Science, 1200 New York Avenue NW, Washington, DC 20005.